communications earth & environment

Article

A Nature Portfolio journal

https://doi.org/10.1038/s43247-025-02926-6

Satellite radar advances carbon emissions accountability over tropical peat

Cheryl Tay[1,2] ✉, A. Jonay Jovani-Sancho[3], Lisna Yulianti[4], Chris Evans[3], Nathan Callaghan[3], Adi Jaya[4], Rino Salman[2], Yujie Zheng[5], Susilo Susilo[6], Salampak Dohong[4] & Sang-Ho Yun[1,2,7]

Carbon markets face growing criticism over unreliable measurements of carbon credits. Tropical peatlands, which contain some of Earth's most concentrated carbon, represent a huge, untapped opportunity for emission reductions, but remain excluded from the market due to challenges in measuring emissions due to degradation. Here, we demonstrate satellite L-band Interferometric Synthetic Aperture Radar as a solution to estimate carbon dioxide emissions by accurately measuring peat subsidence. Our framework accounts for major radar noise sources in tropical environments that were previously unaddressed, and is validated against high-rate ground-measured peat motion in both space and time. The radar results capture episodic peat motion linked to dry-wet cycles across different land uses, and long-term rates accurate up to 0.6 mm yr^{-1}, equivalent to 0.97 t CO_2 ha^{-1} yr^{-1} in emissions. This scalable, cost-effective approach provides a robust tool for Monitoring, Reporting, and Verification, benefitting carbon markets, local regulation, and global climate mitigation efforts.

Robust estimation of carbon emissions from degrading tropical peatlands has been a longstanding challenge. The 2013 Intergovernmental Panel on Climate Change (IPCC) Wetlands Supplement[1] highlighted this issue, noting that Tier 1 emission factors are limited by sparse data availability in tropical regions. While Tier 1 uses generalised emission factors based on land use categories, the report called for more spatially and temporally comprehensive data to develop Tier 2 and Tier 3 emission factors that better capture the complexity of these peat environments. These challenges are further reflected in the carbon market. The uptake of peat-based carbon credits has largely been impeded by a lack of robust data[2]. More broadly, the carbon market has been struggling with the accountability of carbon credits, often relying on questionable or inadequate measurement practices to prove that emissions have been reduced or avoided[3,4]. The scarcity of measurements risks misrepresenting complex environments, especially when extrapolated to large areas, potentially leading to exaggerated or inaccurate valuation of carbon credits[5–7].

Peat motion, or the rise and fall of the peat surface, is a valuable indicator of peat condition, reflecting both the hydrology and carbon balance. Peatlands are concentrated carbon stores, containing around 33% of global soil carbon within 3–4% of global land area[8]. However, they turn into carbon sources when degraded, releasing up to 1 Gt CO_2 yr^{-1} globally due to drainage[1]. Over shorter periods, both natural and human-modified peatlands shrink and swell in response to groundwater fluctuations over dry-wet cycles. Over longer periods, lowered groundwater due to drainage or other forms of degradation lead to subsidence, driven by physical processes of compaction and consolidation, and by peat oxidation, which releases CO_2[9]. Peat motion thus complements groundwater and CO_2 measurements, especially as these data are widely unavailable[10,11]. Peat motion has several applications in Measurement, Reporting, and Verification (MRV), including understanding peat responses to disturbances such as drainage, land use change, and climatic variability[12–16], assessing the effectiveness of rewetting and restoration[17–19], verifying peat-based carbon credits in compliance and voluntary carbon markets[2], and estimating CO_2 emission factors and greenhouse gas inventories[12,20,21].

Interferometric Synthetic Aperture Radar (InSAR) remote sensing offers a unique value for peatland MRV through its spatiotemporal coverage and precision in measuring peat motion. InSAR utilises phase shifts of microwave signals to measure changes in the satellite-to-ground distance with millimetre-scale precision. The advantages include continuous spatial coverage, high spatial resolution, frequent revisits for temporal analysis, and weather- and cloud-independency. These capabilities address challenges faced in peatland MRV, where ground-based sampling is often limited by sparse spatial coverage and infrequent measurements, leading to unreliable measurements and high monitoring costs that limit the effectiveness of regulation[22], uptake of projects in carbon markets[2], and emissions reporting[10,11].

[1]Asian School of the Environment, Nanyang Technological University, Singapore, Singapore. [2]Earth Observatory of Singapore, Nanyang Technological University, Singapore, Singapore. [3]UK Centre for Ecology & Hydrology, Deiniol Road, Bangor, Wales, UK. [4]University of Palangka Raya, Palangka Raya, Indonesia. [5]The University of Texas at Dallas, Richardson, USA. [6]National Agency for Research and Innovation, Jakarta, Indonesia. [7]School of Electrical and Electronic Engineering, Nanyang Technological University, Singapore, Singapore. ✉e-mail: cheryl.taywj@ntu.edu.sg

To date, the success of InSAR as a tropical peatland monitoring tool remains limited. Whilst studies have measured peat motion with C-band InSAR in temperate regions[23,24], C-band's short wavelength makes it challenging in the tropics due to phase ambiguity (i.e., challenge of counting complete phase cycles) when detecting larger peat displacements observed in the region and decorrelation over denser vegetation[25–28]. Consequently, studies have used longer wavelength L-band InSAR, which suffers less from vegetation decorrelation. However, the L-band accuracy has been unproven in the tropics, with no study directly validating InSAR against in-situ peat motion data to date[12,19,25]. Newly available InSAR algorithms, such as for closure phase bias[29] and ionospheric noise[30,31] that are essential for the tropics, also warrant the need to update InSAR-derived peat motions in the region.

Here we present an L-band InSAR framework for mapping tropical peat motion, which is validated both spatially and temporally against ground-truth peat motion data. Using an InSAR framework with improved noise corrections and high-rate field measurements, we address the following key questions: How accurate is InSAR for short- and long-term peat motion? Under what conditions does InSAR perform effectively? Finally, what trends in peat behaviour does InSAR reveal? By addressing these questions, we aim to demonstrate a route towards cost-effective, large-scale peat motion monitoring as a proxy for tropical peatland carbon balance, which is an essential prerequisite for addressing this globally important source of carbon emissions.

Results and Discussion

Peat motion from field measurements

To validate InSAR-derived peat motion, we focused on tropical peatlands of Palangkaraya, Central Kalimantan, Indonesia, where we collected high-resolution field measurements at 8 sites (Fig. 1a). All sites are within or adjacent to the former Mega Rice Project area, where over 1 million hectares of peat swamp forest were deforested and over 4000 km of canals were constructed to drain peat for unsuccessful rice cultivation between 1996 and 1998. Excessive drainage and subsequent partial land abandonment led to dry, scrub-covered peat that is vulnerable to frequent fires, especially during dry seasons[32,33], notably causing major fires in 1997 and 2015[34]. The peatlands now mainly comprise smallholder cropland, smallholder and industrial plantations, scrubland, and secondary forests[35]. Drainage continues through the formerly constructed network of canals and smaller canals subsequently dug (Fig. 1a) to support agricultural activities. This has resulted in rapid, ongoing subsidence driven by compaction, consolidation, and oxidation of the peat, with oxidation also leading to high CO_2 emissions.

Our field measurements showed both high levels of episodic fluctuation in peat surface elevation, linked to dry-wet cycles, and long-term subsidence at drained sites (Fig. 1b). The 8 sites comprise different land uses including oil palm plantations, cropland, fern-dominated scrubland, and secondary forests. Measurements were made using peat cameras between 1 November 2018 and 24 March 2024 following the method of Evans et al.[14]. These timelapse cameras move with the peat surface and capture images of a stable reference point, providing sub-millimetre precision of peat motion at a two-hourly frequency. Short periods of data loss affected all sites in late 2021 and early 2022 but the datum point remained unchanged between measurement periods. Episodic subsidence was observed at most sites during the dry seasons from 2019 to 2023, typically occurring between May and September when minimal rainfall induces lowered groundwater levels (Supplementary Fig. 1). The dry seasons, with <5 mm 30-day mean rainfall recorded at the nearby Tjilik Riwut Airport weather station (2.22°S, 113.95°E, 10 to 65 km away from sites), are highlighted in Fig. 1b. UPR forest

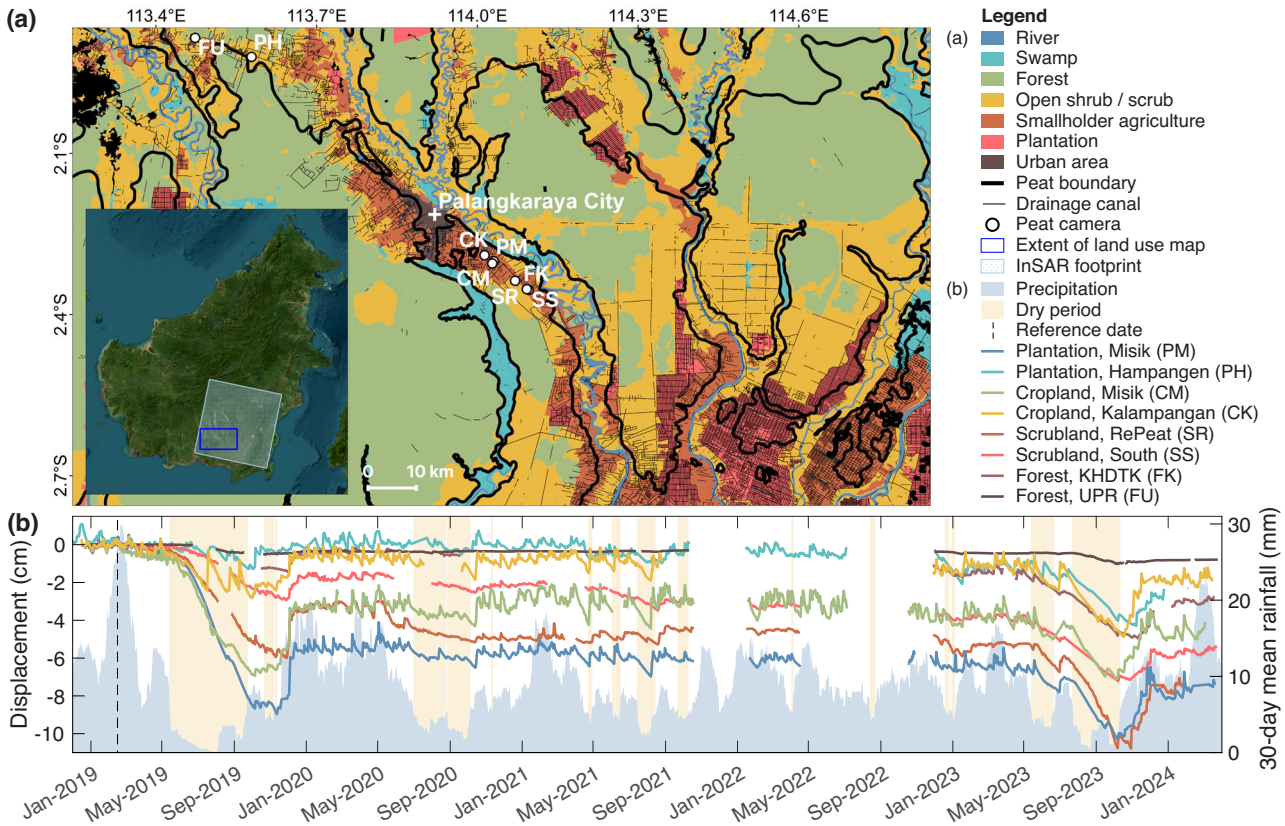

Fig. 1 | Field-measured peat motion in drained peatlands of Palangkaraya, Central Kalimantan, Indonesia. a Land use, drainage canals, peat camera sites, and InSAR coverage (inset). **b** Vertical displacement measured by peat cameras and 30-day mean rainfall recorded at the nearby Tjilik Riwut Airport weather station between 2018 and 2024. Positive and negative values indicate uplift and subsidence, respectively, throughout this study. Dry periods with <5 mm 30-day mean rainfall, typically between May and September, are highlighted.

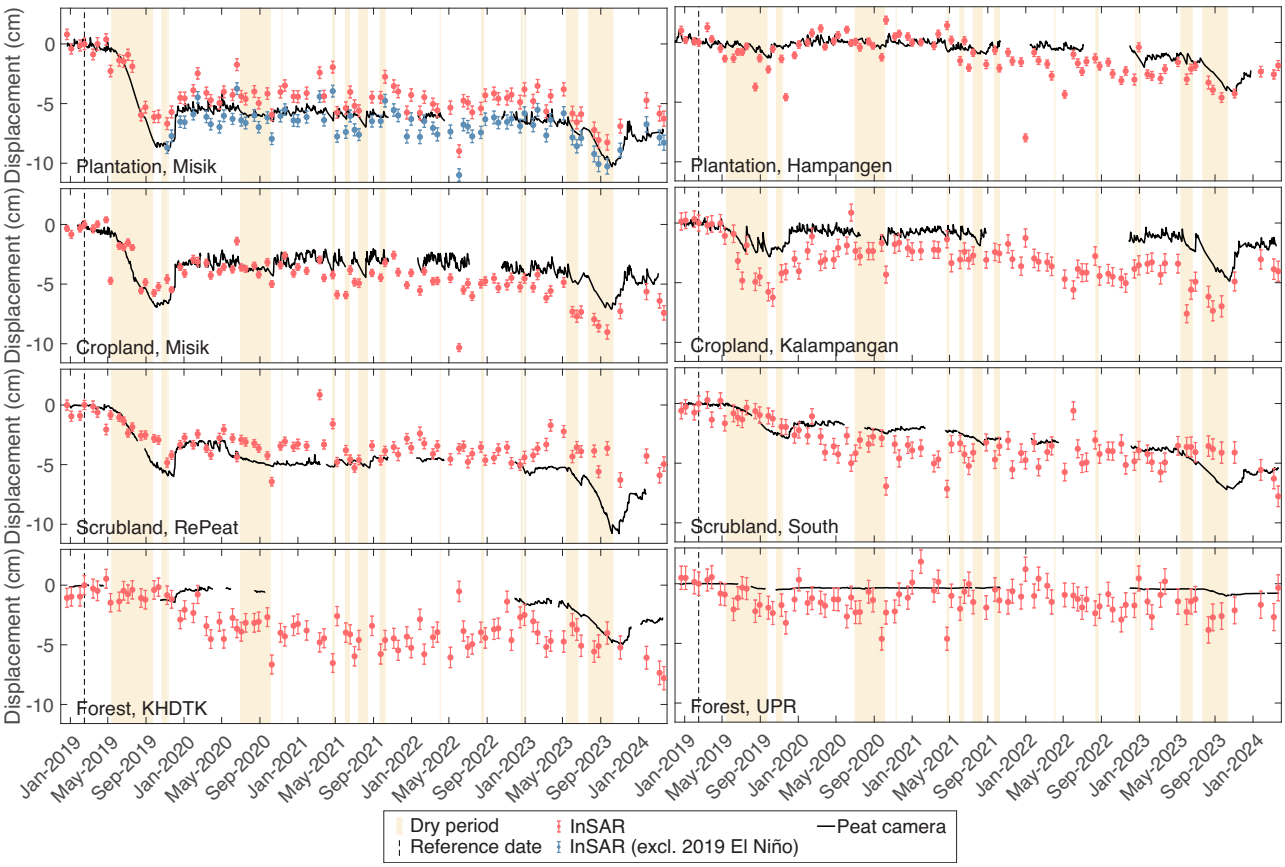

Fig. 2 | Comparison of InSAR-derived peat motions against peat camera field measurements. InSAR captured both long-term subsidence and episodic fluctuations in peat motion at several field validation sites. InSAR displacements were projected from the line-of-sight to the vertical direction. Error bars indicate the InSAR phase standard deviation, σ_ϕ, which was derived from coherence that was propagated through the inversion matrix used for time series analysis. The peat camera at Misik plantation likely detected stronger, localized subsidence compared to its surroundings during the 2019 El Niño – a downshifted InSAR time series shows better fit with peat camera displacements after the 2019 El Niño.

did not subside in most years as it was flooded most of the time based on groundwater levels (Supplementary Fig. 1) and field observations[14]. The largest episodic subsidence, up to 8 cm, occurred in 2019 and 2023 during dry seasons. These subsidence events coincided with positive phases of the National Oceanic and Atmospheric Administration Oceanic Niño Index[36] and were thus likely intensified by the interannual El Niño[14], which causes drought-like conditions every few years in the region[33,37]. Both events were followed by several centimetres of uplift, coinciding with the onset of rain. However, rebounded peat surface elevations were lower than before the dry seasons despite similar groundwater levels, suggesting permanent peat loss due to oxidation, or irreversible compaction and consolidation due to drying[14].

Validation of InSAR peat motions

Using ALOS-2 ScanSAR imagery acquired between 12 October 2018 and 9 August 2024, we derived displacement time series, which show peat motion at each acquisition date and its evolution over time, and estimated the corresponding long-term rates, which represent the average displacement per year over the full observation period. ALOS-2 is a Japanese L-band radar satellite capable of providing repeat observations every 14 days in ScanSAR mode, with 350 km x 350 km coverage per image. Using an InSAR time series analysis approach (see Methods), we produced spatially continuous measurements at 180 m x 180 m spatial resolution across Central Kalimantan (Fig. 1).

Our L-band InSAR results captured episodic fluctuations observed in field measurements at the majority of the sites, including plantations, cropland, and scrubland. Large subsidence and rebound during and after both El Niño dry seasons, and greater stability during non-El Niño periods were similarly observed in InSAR (Fig. 2). The average root mean squared error (RMSE) and Pearson's correlation coefficient (r) between epoch-to-epoch displacements of the peat cameras and InSAR were 1.70 ± 0.31 cm and 0.75 ± 0.09 across these 6 sites, and 1.75 ± 0.34 cm and 0.70 ± 0.14 across all sites, including forest sites (Table 1a, b). The lowest RMSE was 1.27 cm at Hampangen plantation, and the highest r was 0.88 at Misik plantation (Table 1a, b). The sites where InSAR performed less well were Kalampangan cropland (high RMSE of 2.21 cm, but high r of 0.83) and UPR forest (low r of 0.40, but low RMSE of 1.55 cm). In both cases, InSAR captured the long-term trend, showing subsidence at the cropland site and no change at the forest site, but overestimated the amount of short-term motion compared to observed values (Fig. 2). At the second forest site at KHDTK, a long data gap in the peat camera data precluded a full assessment of short-term variations.

Our L-band InSAR results also closely matched long-term, multi-annual rates of peat motion measured in the field. Both the peat cameras and InSAR showed rates around −1 to 0 cm yr^{-1} across all sites over 5.5 years (Table 1c, d, negative values indicate subsidence throughout). The smallest absolute difference between peat camera and InSAR rates was 0.06 cm yr^{-1} at UPR forest, and the largest was 0.59 cm yr^{-1} at RePeat scrubland (Table 1e). The RMSE of the rates across the 8 sites was 0.36 cm yr^{-1}, with no overall tendency of InSAR to underestimate or overestimate the rates. To the best of our knowledge, no tropical peatland study has directly compared InSAR with in-situ field-measured peat motion. For example, previous studies only compared overall InSAR and field-measured peat motion ranges without site-to-site validation[12,28], or compared InSAR indirectly

Table 1 | InSAR accuracy against peat camera field measurements

#	Land use	Peat camera site	Displacements (cm)		Long-term rates (cm yr^{-1})			(f) Mean σ_ϕ (cm)
			(a) RMSE	(b) *r*	(c) Peat camera	(d) InSAR	(e) Difference	
1	Oil palm plantation	Misik	1.73	0.88	−0.98	−0.76	−0.23	0.52
		Misik (excl. 2019 El Niño)	1.02	0.71	−0.58	−0.43	−0.15	0.54
2	Oil palm plantation	Hampangen	1.27	0.69	−0.43	−0.67	0.24	0.68
3	Cropland	Misik	1.63	0.73	−0.41	−0.96	0.55	0.37
4	Cropland	Kalampangan	2.21	0.83	−0.32	−0.69	0.37	0.56
5	Fern-dominated scrubland	RePeat	1.83	0.69	−1.12	−0.53	−0.59	0.43
6	Fern-dominated scrubland	South	1.56	0.67	−1.06	−0.80	−0.26	0.73
7	Secondary forest	KHDTK	2.25	0.68	−0.64	−0.85	0.21	0.83
8	Secondary forest	UPR	1.55	0.40	−0.11	−0.18	0.06	0.89
	Overall		1.75 ± 0.34	0.70 ± 0.14	-	-	0.36	-
	Overall (excl. forests)		1.70 ± 0.31	0.75 ± 0.09	-	-	0.40	-

[a, b]RMSE and *r* were computed between epoch-to-epoch displacements of InSAR and peat cameras.
[c, d, e]Differences in the long-term, multiannual rates were computed from the peat camera velocity minus the InSAR velocity.
[f]Lower mean InSAR phase standard deviation, σ_ϕ indicates better ease of tracking motion for an InSAR pixel.
InSAR motions were projected from the line-of-sight to the vertical direction for all calculations.

against peat motion inferred from in-situ groundwater levels[25]. Our results therefore, demonstrate accuracy and represent the most direct one-to-one field validation of InSAR-derived peat motion in the region thus far.

Deviations between InSAR and field measurements are expected, given their differing spatial and temporal resolutions. InSAR detects average peat motions within 180 m x 180 m pixels, while field measurements are point-based. Deviations thus arise from local-scale heterogeneity, especially in heavily managed areas where varying management or proximity to ditches causes varying subsidence within an image pixel. At Misik plantation, nearby manual subsidence pole measurements showed less subsidence than at the peat camera post-2019 El Niño and aligned better with InSAR (Supplementary Fig. 2). InSAR may thus accurately reflect the landscape-average subsidence, rather than faster subsidence at the specific camera location during the 2019 El Niño. Excluding the 2019 El Niño, InSAR showed high consistency in RMSE and *r* with the peat camera (Fig. 2, Table 1). Next, ALOS-2's 14- or 28-day revisit interval is better suited for detecting longer-term trends over months, such as from El Niño dry seasons and persistent drainage effects. Shorter fluctuations are less detectable, such as three rapid uplift episodes at Kalampangan cropland in 2019, which corresponded to irrigation timings[14] (Fig. 2).

The higher InSAR accuracy estimations given above are achieved through robust noise reduction, which was unaccounted for in previous studies. The ionospheric noise was up to 6.7 m, averaging 2.3 ± 1.5 m between any two points across the 350 km x 350 km ALOS-2 image (Supplementary Fig. 6b). We used a range split-spectrum correction[30,31] which better captures the spatial complexity of ionospheric noise (Supplementary Fig. 6) as opposed to ad-hoc use of linear or quadratic detrending in previous studies[12,15,19,25]. The closure phase bias caused up to 30 cm of cumulative false subsidence over 5.5 years, especially over scrubland and forests (Supplementary Fig. 7a). We used a larger temporal network of interferograms than previous studies[12,15,19,25] and an additional correction of Zheng et al.[29] to reduce the bias. Tropospheric noise was up to 15 cm at any given time (Supplementary Fig. 8). Corrections using global atmospheric models in previous studies[12,15,19,25] led to worse or no change in the RMSE and *r* of rates and displacements compared to without correction, while our correction based on spatially correlated noise characteristics improved the performance across all sites (Supplementary Table 1).

The sub-centimetre accuracy in L-band InSAR long-term rates with corrections applied as outlined above could significantly improve peat carbon emission estimations. A widely used method by Couwenberg & Hooijer[20] converts subsidence rates to CO_2 emissions by relating subsidence to changes in anoxic peat thickness (see Methods). Based on this approach, the long-term rate accuracy of up to 0.06 cm yr^{-1} translates to 0.97 t CO_2 ha^{-1} yr^{-1} of uncertainty in CO_2 emissions, assuming all subsidence is due to peat oxidation. This assumption is appropriate for long-drained peatlands where oxidation dominates subsidence, such as the Mega Rice Project area analysed here, but does not apply to recently drained peatlands where compaction and consolidation dominate subsidence. The sub-centimetre accuracy, at least two orders of magnitude smaller than major InSAR noises unaccounted for in prior studies, thus enhances reliability in estimating CO_2 emissions from peat motion. Additionally, this level of accuracy is achieved cost-effectively and over a large area across sites, overcoming practical limitations of ground-based measurements such as subsidence poles, flux towers, and chambers. Current carbon emission reporting frameworks rely heavily on point-based ground measurements, like in the case of Tier 1 emission factors in the 2013 IPCC Wetlands Supplement[1]. Achieving broad coverage with these methods is costly and labour-intensive. Subsidence poles, in particular, require numerous readings to derive an accurate measurement that accounts for human error and variability due to micro-topography within a single site[38]. In contrast, the InSAR accuracy demonstrated here may be upscaled with ease and thus offers a practical solution for site- to regional-scale carbon emission estimates.

Variability and drivers of peat motion

We found high variability in long-term rates of subsidence within similar land uses and drainage intensities; this underpins the value of InSAR for refining carbon emissions, since no single environmental factor strongly predicts peat motion. Extending our analysis to all peatlands of Central Kalimantan, we observed large overlap and similar mean long-term rates across land uses (Fig. 3c). Correlations of long-term rates with distance from the peat edge ($r = 0.16$, Fig. 3d) and with drainage canal density ($r = -0.20$, Fig. 3e) were weak. A possible interpretation is that greater drainage density leads to higher subsidence rates, as expected, but that areas close to the peat edge tend to have thinner peat and therefore subside less, or remain stable if most peat has been lost. The weak correlations may reflect a combination of high local-scale variations in land management, InSAR measurement uncertainties, land use classification errors, or unquantified impacts of water management. For example, one study suggested that differing canal depths and flow control structures likely influence peat motions more than drainage density in the former Mega Rice Project area[13]. As rewetting efforts gain traction, variations in water management could further accentuate peat motion variability. If water management is indeed influencing the InSAR results, this would imply that the method has the potential to monitor changes in peat condition due to interventions such as peat re-wetting, though further analysis using data from areas with known water table changes is needed.

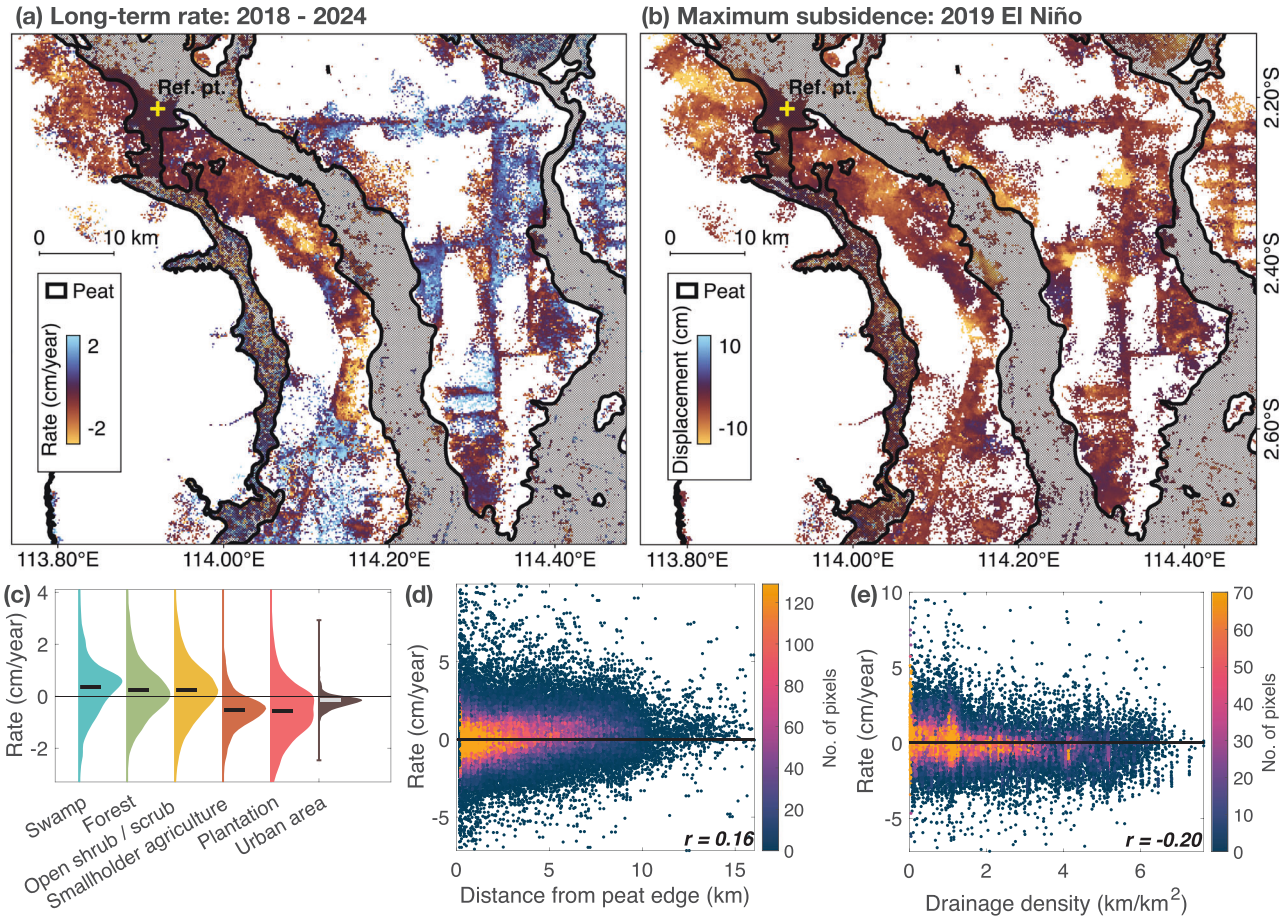

Fig. 3 | Large-scale trends in InSAR-derived peat motions and their correlation with different environmental factors. a, **b** Areas that subsided more during the 2019 El Niño did not necessarily subside more in the long term. Long-term rates showed weak correlation with **c** land use, where centre bold lines refer to the mean, **d** proximity from the peat edge, and **e** drainage canal density. All InSAR motions were projected from the line-of-sight to vertical direction and are relative to a stable reference point in the city centre of Palangkaraya. Areas with high mean InSAR phase standard deviation, $\sigma_\phi > 0.7$ cm were excluded from the analysis.

Over shorter timescales, the InSAR displacements provide insights into the peat's response to disturbances and recovery. During the 2019 El Niño, all land uses experienced subsidence (Fig. 3a), but several swamp, forest, and scrubland areas fully rebounded after the dry season, with no long-term subsidence (Fig. 3b). In contrast, cropland and plantations showed partial rebound, implying irreversible subsidence and long-term peat loss. Within each land use, areas with less subsidence during El Niño do not necessarily experience less long-term subsidence (Supplementary Fig. 3). These could again be due to localised differences in drainage intensity and water management[13], or because peat in less degraded sites retains greater elasticity to respond to dry-wet cycles. This elasticity helps natural peatlands stay wetter during droughts and was observed in intact Sumatran forests, while drained plantations showed less short-term variability but faster long-term subsidence[39]. As with high-latitude peatlands, InSAR's ability to track seasonal and short-term motion in tropical peatlands may serve as a diagnostic tool for assessing peat condition and associated CO_2 emissions[40].

The high spatial and temporal variabilities in peat motions found above underscore the benefit of direct, location-specific monitoring of heterogeneous tropical peat landscapes through L-band InSAR. Conventional approaches rely on sparse measurements, such as subsidence poles, and use proxies, such as land use or drainage intensities shown above, to extrapolate and estimate CO_2 emissions over large areas. These proxies cannot capture fine-scale spatial or temporal variations in peat motion that InSAR reveals and may lead to under- or over-estimation of CO_2 emissions. In contrast, the InSAR framework here would provide continuous coverage and direct measurements across heterogeneous peatlands, reducing reliance on proxies, generalised assumptions, or static measurements, and enabling more accurate and comprehensive emission estimates.

Conclusions

In conclusion, we demonstrated an L-band InSAR approach that accurately captures episodic and interannual peat motion trends in the tropics, with direct validation against high-rate, field-measured peat motion. Although the temporal resolution of ALOS-2 limits the investigation of shorter-term trends, newer L-band satellites like ALOS-4 and NISAR will overcome this in the coming years. Our framework targets degraded parts of peatlands, where CO_2 emissions are highest, and monitoring is most needed. The results here will benefit peatland MRV, filling gaps in existing approaches that lack spatial and temporal coverage. InSAR also provides a source- and location-specific proxy for belowground peat degradation, complementing broader atmospheric CO_2 measurements such as from flux towers and satellite spectrometers. Accuracy and scalability from InSAR are crucial, especially as Southeast Asia sees a rise in carbon markets such as IDX Carbon (Indonesia) and Climate Impact X (Singapore), where robust peatland MRV is essential for transparency. Because these markets build upon widely established or recognised protocols for carbon emission estimations, such as those that have been used for IPCC reporting, integrating InSAR measurements into these protocols would enhance the robustness of emission estimates and improve the integrity of both scientific reporting and carbon market accounting. With peat management and restoration recognized as key to meeting global CO_2 emissions reduction targets, the InSAR framework here offers a cost-effective and scalable solution for supporting these critical efforts.

Methods

InSAR analysis

We used 92 PALSAR-2 ALOS-2 ScanSAR L1.1 images acquired between 12 October 2018 and 9 August 2024, along Path 28, Frame 3650. To derive displacements, we first used the alosStack module[30] in the InSAR Scientific Computing Environment (ISCE) v2.6.3 software[41] to resample images to a common grid using the 19 June 2020 image as the reference, interfere images to form interferograms, perform ionospheric corrections, and multi-look, filter, and unwrap interferograms. We multi-looked the interferograms by 17 and 56 in range and azimuth directions, respectively, resulting in pixel sizes of around 180 m x 180 m after geocoding.

We then used the Miami InSAR time-series software in Python (MintPy) v1.5.3 software[42] to perform Small BAseline Subset (SBAS) network inversion to solve for stepwise displacements between images, correct for solid Earth tides (SET) and closure phase biases, and geocode the time series result. Pixels from all interferograms were included and weighted by the inverse of phase covariance[43,44] for the SBAS network inversion, which ensures that noisy pixels are downweighted. For post-processing analyses relating to land uses, distances from peat edge, and drainage canal densities, we excluded pixels with a high mean phase standard deviation ($\sigma_\phi > 0.7$ cm) to improve robustness of the analyses. SET refers to the deformation of the Earth's crust caused by the gravitational attraction of the moon, Sun, and other celestial bodies. To remove these non-peat displacements, we applied MintPy's SET correction, which uses PySolid[45,46] to estimate the tidal deformation at each location and image acquisition time based on Love numbers and celestial ephemerides. Finally, we corrected the geocoded time series for spatially correlated tropospheric noise using an independent algorithm described in a later section. We did not apply the topographic residual correction in MintPy as the ALOS-2 orbits are well controlled with typical perpendicular baselines of ALOS-2 data between 100 m and 500 m relative to the reference image (Supplementary Fig. 4). These result in small height ambiguities where the topographic residual correction is not critical[47].

The reference point of the InSAR analysis was collocated with the CPKY Global Navigation Satellite System (GNSS) station located in the urban area of Palangkaraya (−2.220°,113.926°). The station is stable, with a vertical velocity of <1 mm yr^{-1} from 2018 to 2024, based on a GNSS time series processed following the method of Susilo et al.[48]. To ensure a fair comparison between peat cameras and InSAR, we projected the line-of-sight InSAR displacements and rates to the vertical by dividing the cosine of pixel-wise local incidence angles. We detail the parameters that led to large reductions in noise in the derived displacements and rates in the following sections.

Ionospheric noise correction

We estimated the ionospheric phase using the range split-spectrum approach in the alosStack module[30,31]. We heavily multi-looked interferograms by 80 and 448 in range and azimuth, respectively, to improve the signal-to-noise ratio, while still maintaining sufficient detail to estimate the long-wavelength ionospheric phase. The correction is most robust over areas that suffer from minimal decorrelation. Thus, we only used bandwidth-4 interferograms, which maintain reasonable coherence over most pixels, to solve for the ionospheric contribution of each individual image. We define the bandwidth as the maximum temporal separation used to pair images to form the network of interferograms. In a bandwidth-4 interferogram network, for example, each image is paired with the next 4 images acquired after itself to form 4 different interferograms. The bandwidth is thus agnostic to the number of days between images. We also removed decorrelated areas when estimating the ionospheric phase, then rely on the spatial interpolation of the estimated ionospheric phase to fill gaps over decorrelated areas. These decorrelated areas often occur over rivers and water bodies that may not be captured in the water body dataset from the Shuttle Radar Topography Mission[49]. An example of an improved ionospheric correction due to the removal of decorrelated areas is shown in Supplementary Fig. 5. Supplementary Fig. 6 shows the offsets in displacement caused by ionospheric noise for each date when an image was acquired.

Closure phase bias correction

Closure phase bias refers to the discrepancy amongst triplets of phases (ϕ), where $\phi_{AC} - \phi_{AB} - \phi_{BC} \neq 0$ and A, B, and C are different time epochs. The bias is most prominent in a small bandwidth interferogram network[50] likely because of short-lived signals such as vegetation and soil moisture changes that may cause inconsistency within phase triplets[51,52]. To minimize the effect of closure phase biases, we used (1) a redundant number of interferograms from a bandwidth-20 network, weighted by σ_ϕ^2 for the SBAS network inversion, and (2) a correction method following Zheng et al.[29] in MintPy. An infinitely large bandwidth is most ideal to minimize the effects of closure phase bias, as demonstrated by several studies based on C-band Sentinel-1 images[29]. However, this is not practical for tropical peatlands even with L-band ALOS-2 images, which decorrelate faster with increasing bandwidth due to the longer temporal baselines, commonly of 14, 28 days, or more, as compared to 6 or 12 days for Sentinel-1. Large bandwidths are also not practical for most areas in the tropical peatlands, where coherence is already low, and large bandwidth interferograms would be mostly decorrelated. The inclusion of decorrelated interferograms will then have an insignificant impact on the SBAS network inversion since the interferograms are weighted by σ_ϕ^2. We thus increased the number of bandwidths used only up to 20, where we observed convergence of the SBAS network inversion (Supplementary Fig. 7). This is computationally efficient and also maximizes the performance of the closure phase bias correction of Zheng et al.[29]. As shown in Supplementary Fig. 7, the closure phase bias is continually reduced with increasing number of bandwidths used, especially for the initial smaller bandwidths. The correction is also most critical over scrubland and forests, which experience the largest bias, followed by cropland, then plantations (Supplementary Fig. 7). Finally, the quality of the estimated closure phase depends on the coherence and cannot be reliably estimated if the data is decorrelated. We thus applied different levels of closure phase bias correction for each pixel to avoid introducing unwrapping errors during the correction – using smaller bandwidths to estimate the bias for pixels which decorrelate faster, and larger bandwidths for those which decorrelate slower.

Spatially correlated tropospheric noise correction

Tropospheric noise may have magnitudes up to tens of centimetres[53,54]. It is spatially correlated over varying distances of a few to tens of kilometres[53,55], but temporally uncorrelated over a few hours or less[55]. The wet (turbulent) tropospheric component, driven by differential spatial variations in water vapour, contributes noise across a broad range of spatial scales from a few to tens of kilometres, as turbulent processes cascade energy from large atmospheric motions to smaller scales. The dry (hydrostatic) component varies more smoothly with pressure and temperature, and can also be modulated by elevation-dependent water vapour[55]. In our study area, spatially correlated tropospheric noise is dominant as observed from anomalous values of up to 15 cm in the InSAR time series that occur at the same time epoch across several InSAR pixels that are located close to each other (Supplementary Fig. 8). For example, Hampangen plantation and UPR forest are just a few kilometres apart, while the other 6 sites form a separate, closely located group. Each group shares the same peaks in their time series (Supplementary Fig. 8). We found that corrections based on global atmospheric models (GAMs) such as PyAPS and GACOS worsened the InSAR accuracy, while corrections based on height correlation were not effective for reducing these tropospheric effects (Supplementary Table 1). This is likely because of the low resolution of the atmospheric variables in GAMs, which are not suited for removing turbulent tropospheric noise[56–58]. Since the terrain around the Palangkaraya peatlands is mostly flat, the elevation-dependent tropospheric noise is not dominant, as the thickness of the troposphere that the InSAR microwave propagates through is almost

constant[56,57]. Common scene stacking corrections, which rely on temporal averaging of numerous scenes to reduce noise, were also inapplicable due to the low frequency of revisits of ALOS-2.

Instead, we reduced the spatially correlated tropospheric noise at each pixel by utilizing the stacked time series of neighbouring non-deforming pixels. Based on the assumption that tropospheric noise is spatially correlated, the signals at non-deforming pixels ($\phi^{non-def}$) close to each other would contain predominantly tropospheric noise that is similar across pixels, and to a smaller extent other random noise that may be dissimilar across pixels:

$$\phi^{target} = \phi^{target}_{def} + \phi^{target}_{tropo} + \phi^{target}_{noise} \quad (1)$$

$$\phi^{non-def} = \phi^{non-def}_{tropo} + \phi^{non-def}_{noise} \quad (2)$$

ϕ^{target} refers to the phase of a target pixel which we want to remove the tropospheric noise from. Thus, stacking the time series of these neighbouring non-deforming pixels, by taking the mean, would amplify the spatially correlated tropospheric noise while cancelling out other random noise. This results in an approximation of the spatially correlated tropospheric noise around a target pixel that can then be removed from the target pixel itself:

$$\phi^{target}_{tropo} \approx \frac{1}{k}\left(\sum_{i=1}^{k} \phi^{non-def,i}\right), \text{where all } \phi^{non-def} \textit{ are close to } \phi^{target} \quad (3)$$

We applied this noise correction for each pixel independently. We defined non-deforming neighbouring pixels as those with a velocity of less than 1 mm yr^{-1} over the whole time series, an average spatial coherence above 0.3, and a maximum distance of 10 km away from the target pixel. The maximum distance was selected to be within typical spatial correlation lengths of wet tropospheric noise of not more than tens of kilometres[53,55]. A future improvement may be to use adaptive distances for each target pixel based on spatial correlation metrics, but we find a maximum 10 km distance sufficient for removing large-magnitude tropospheric signals in this study area (Supplementary Fig. 8). Finally, only target pixels with at least 5 non-deforming neighbouring pixels were corrected for the spatially correlated tropospheric noise to avoid the inclusion of other random noise. The correction improved the average RMSE and r between InSAR and peat camera epoch-to-epoch displacements, while the RMSE of long-term rates was mostly unaffected (Supplementary Table 1). The reduced noise in the time series is also shown by the smaller number of anomalous values for all sites (Supplementary Fig. 8).

Phase variance and standard deviation

We used the phase variance, σ^2_ϕ or standard deviation, σ_ϕ to indicate the quality of InSAR measurements (Table 1f, Fig. 2). σ^2_ϕ is estimated from the coherence, γ, for each InSAR pixel following Eq. 4[55], where γ refers to the similarity between two SAR images acquired on different dates:

$$\sigma^2_\phi = \frac{1-\gamma^2}{2N\gamma^2} \quad (4)$$

Where γ is higher, σ^2_ϕ and σ_ϕ are lower, and the InSAR phase is more similar between images, facilitating more reliable displacement tracking. σ_ϕ of each date in the displacement time series (Fig. 2) was estimated via linear propagation of σ_ϕ of each interferogram used during the SBAS network inversion. The mean σ_ϕ in Table 1f was then derived from the mean of all σ_ϕ of each date over the entire displacement time series.

InSAR captured the episodic fluctuations in peat motion better at peat camera sites when σ_ϕ is lower. The mean σ_ϕ ranged from 0.37 cm to 0.73 cm across non-forested sites, where InSAR performed better and exceeded 0.80 cm at forest sites, where InSAR performed worse (Table 1f, Fig. 2) due to several expected causes of coherence loss: Firstly, forest sites have dense, multi-layered vegetation structures that typically cause strong volume scattering and thus coherence loss. Secondly, vegetation growth causes temporal decorrelation while also increasing volume scattering. The South scrubland (mean σ_ϕ of 0.73 cm), for example, was initially covered in short vegetation in late 2018, but later consisted of trees and taller vegetation in later years due to forest regrowth. Thirdly, longer than usual time gaps between images further decrease coherence at any site, such as from mid 2023 to early 2024 where the area was imaged every 42 to 84 days instead of 14 to 28 days. σ_ϕ is thus expected to be higher at forest sites and to varying degrees, scrubland, compared to the plantation and cropland sites. Similar variations in σ_ϕ also extend beyond the peat camera sites across the analysed peat area in Central Kalimantan, where the mean σ_ϕ was often higher over forests than other land uses (Supplementary Fig. 9). However, σ_ϕ still varies widely within each land use (Supplementary Fig. 9) and is a more reliable indicator of the InSAR measurement quality than the generic land use alone.

Conversion of peat motions to carbon emissions

We used the method of Couwenberg & Hooijer[20] which has been applied in several tropical peatland studies[12,21] to approximate the amount of carbon emissions (t CO_2 ha^{-1} yr^{-1}) from peat motion rates as follows:

$$CO_2\text{emission} = \text{subsidence rate} \times \text{dry bulk density} \times \text{carbon concentration} \times 3.67 \quad (5)$$

We used long-term InSAR subsidence rates, carbon concentration of 55% and dry bulk density of 0.08 g cm^{-3} which are mean values across Southeast Asia peatlands[12], and a C to CO_2 conversion factor of 3.67. The equation assumes that all subsidence is due to peat oxidation, but may be scaled if a portion of the total subsidence should be attributed to compaction and consolidation. A higher percentage of subsidence due to oxidation would be more reflective of peat that was drained longer before, where most compaction and consolidation have already occurred during the initial stages of drainage. For simplicity, we assumed that all measured subsidence reflects oxidation, which is appropriate for long-drained areas such as our study area, but not for recently drained areas where compaction and consolidation will dominate.

Analysis of environmental factors

We referred to 2023 maps for land uses obtained from the Ministry of Environment and Forestry of Indonesia. For simplicity, we aggregated land uses into broad categories of swamp, forest (primary and secondary dry land, mangrove and swamp forests, and plantation forests), open shrub/scrub (open land, shrubs, and swamp shrubs), smallholder agriculture (dry land and mixed dry land farming, and rice fields), plantation, and urban area (port, transmigration, and settlement areas). Actual land uses at the peat cameras are based on field observations[14] and may differ from the land use maps.

The boundary of peatlands in Central Kalimantan within the ALOS-2 image and distances of each InSAR pixel to the peat edge were determined from peat maps as of 2019 from the Indonesian Soil Research Institute.

To compute drainage canal densities, we used published drainage canal maps derived from optical imagery acquired by PlanetScope CubeSat sensors between July and September 2017 and processed using a convolutional neural network[13]. We converted the maps from a binary raster format to a line vector shapefile format, then used the shapefile to sum the length of drainage canals at a resolution of 1 km to obtain drainage canal densities in units of km per km^2 – following a similar convention used in the original publication[13]. Finally, we resampled the lower-resolution (1 km) raster of drainage canal densities to the same grid as the higher-resolution (180 m) raster of InSAR peat motion rates to compute the pixel-to-pixel correlation between the two.

Reporting summary

Further information on research design is available in the Nature Portfolio Reporting Summary linked to this article.

Data availability

Peat motions derived from ALOS-2 InSAR presented in this study are available in the following DR-NTU Data repository: https://doi.org/10.21979/N9/JGQE4O. Peat camera data were obtained under a research permit (No. 2151/FRP/E5/Dit.KI/IV/2018, dated 11 April 2018) granted to A.J.J.-S. by the Ministry of Research Technology and Higher Education of Indonesia (RISTEKDIKTI), now National Research and Innovation Agency (BRIN), and directly from the University of Palangkaraya and Centre for International Co-operation in Sustainable Management of Tropical Peatland (CIMTROP) managed by L.Y. and A.J.J.-S. Access to the peat camera data requires a valid research permit from BRIN and a formal request to both BRIN and CIMTROP (contact through adijaya@agr.upr.ac.id), in accordance with Indonesian research regulations. Land use and peat maps were obtained through and should be requested from the Ministry of Environment and Forestry of Indonesia and Indonesian Soil Research Institute, restricted to approved research purposes. The drainage canal maps were obtained from the original publication of Dadap et al.[13] and are publicly available from https://doi.org/10.25740/yj761xk5815. Precipitation data were obtained from the Meteorology, Climatology, and Geophysical Agency of Indonesia (BMKG) and are publicly available from the BMKG Data Online portal https://dataonline.bmkg.go.id/ through free user registration and login.

Code availability

InSAR processing software, including ISCE v2.6.3 and MintPy v1.5.3 are open-source and freely available through GitHub.

Received: 3 June 2025; Accepted: 17 October 2025;
Published online: 26 November 2025

References

1. Hiraishi, T. et al. 2013 Supplement to the 2006 IPCC Guidelines for National Greenhouse Gas Inventories: Wetlands. *IPCC Switz.* (2014).
2. Bonn, A. et al. Investing in nature: Developing ecosystem service markets for peatland restoration. *Ecosyst. Serv.* **9**, 54–65 (2014).
3. Lakhani, N. Revealed: top carbon offset projects may not cut planet-heating emissions. *The Guardian* https://www.theguardian.com/environment/2023/sep/19/do-carbon-credit-reduce-emissions-greenhouse-gases (2023).
4. Temple, J. The growing signs of trouble for global carbon markets. *MIT Technol. Rev.* https://www.technologyreview.com/2023/11/02/1082765/the-growing-signs-of-trouble-for-global-carbon-markets/ (2023).
5. Dawes, A. What's Plaguing Voluntary Carbon Markets? *Center for Strategic and International Studies (CSIS)* https://www.csis.org/analysis/whats-plaguing-voluntary-carbon-markets (2024).
6. Earth Finance. How carbon measurement uncertainty is impeding carbon market viability. https://www.earthfinance.com/insights/carbon-measurement-uncertainty (2023).
7. White, N. Bogus Carbon Credits are a 'Pervasive' Problem, Scientists Warn. *TIME* https://time.com/6264772/study-most-carbon-credits-are-bogus/ (2023).
8. Global Peatlands Initiative. Global Peatlands Assessment: The State of the World's Peatlands. *U. N. Environ. Programme Nairobi Kenya* https://doi.org/10.59117/20.500.11822/41222 (2022).
9. Hooijer, A. et al. Subsidence and carbon loss in drained tropical peatlands. *Biogeosciences* **9**, 1053–1071 (2012).
10. Hoyt, A. M., Chaussard, E., Seppalainen, S. S. & Harvey, C. F. Quantifying Subsidence in Tropical Peatlands. in *Remote Sensing for Characterization of Geohazards and Natural Resources* 347–357 (Springer, 2024).
11. Minasny, B. et al. Mapping and monitoring peatland conditions from global to field scale. *Biogeochemistry* **167**, 383–425 (2024).
12. Hoyt, A. M., Chaussard, E., Seppalainen, S. S. & Harvey, C. F. Widespread subsidence and carbon emissions across Southeast Asian peatlands. *Nat. Geosci.* **13**, 435–440 (2020).
13. Dadap, N. C. et al. Drainage canals in Southeast Asian peatlands increase carbon emissions. *AGU Adv* **2**, e2020AV000321 (2021).
14. Evans, C. D. et al. A novel low-cost, high-resolution camera system for measuring peat subsidence and water table dynamics. *Front. Environ. Sci.* **9**, 630752 (2021).
15. Umarhadi, D. A. et al. Tropical peat subsidence rates are related to decadal LULC changes: Insights from InSAR analysis. *Sci. Total Environ.* **816**, 151561 (2022).
16. de la Barreda-Bautista, B. et al. Exploring Spatial Patterns of Tropical Peatland Subsidence in Selangor, Malaysia Using the APSIS-DInSAR Technique. *Remote Sens* **16**, 2249 (2024).
17. Hooijer, A. et al. Benefits of tropical peatland rewetting for subsidence reduction and forest regrowth: results from a large-scale restoration trial. *Sci. Rep.* **14**, 10721 (2024).
18. Ritzema, H., Limin, S., Kusin, K., Jauhiainen, J. & Wösten, H. Canal blocking strategies for hydrological restoration of degraded tropical peatlands in Central Kalimantan, Indonesia. *Catena* **114**, 11–20 (2014).
19. Zhou, Z., Li, Z., Waldron, S. & Tanaka, A. InSAR Time Series Analysis of L-Band Data for Understanding Tropical Peatland Degradation and Restoration. *Remote Sens* **11**, 2592 (2019).
20. Couwenberg, J. & Hooijer, A. Towards robust subsidence-based soil carbon emission factors for peat soils in south-east Asia, with special reference to oil palm plantations. *Mires Peat.* **12**, 1–13 (2013).
21. Sari, N., Hayati, N., Uzzulfa, M. A., Arief, R. & Krisna, T. C. Mapping carbon dioxide (CO_2) emissions from peat subsidence using carbon parameters and InSAR observations in south Kalimantan, Indonesia. *Soil Sci. Annu*. **74**, 169656 (2023).
22. Evans, C. D. et al. Overriding water table control on managed peatland greenhouse gas emissions. *Nature* **593**, 548–552 (2021).
23. Conroy, P. et al. Probabilistic estimation of InSAR displacement phase guided by contextual information and artificial intelligence. *IEEE Trans. Geosci. Remote Sens.* **60**, 1–11 (2022).
24. Hrysiewicz, A. et al. Estimation and validation of InSAR-derived surface displacements at temperate raised peatlands. *Remote Sens. Environ.* **311**, 114232 (2024).
25. Umarhadi, D. A. et al. Use of multifrequency (C-band and L-band) SAR data to monitor peat subsidence based on time-series SBAS InSAR technique. *Land Degrad. Dev.* **32**, 4779–4794 (2021).
26. Marshall, C. et al. Monitoring tropical peat related settlement using ISBAS InSAR, Kuala Lumpur International Airport (KLIA). *Eng. Geol.* **244**, 57–65 (2018).
27. Izumi, Y. et al. Temporal Subset SBAS InSAR Approach for Tropical Peatland Surface Deformation Monitoring Using Sentinel-1 Data. *Remote Sens* **14**, 5825 (2022).
28. Tarigan, S., Kristanto, Y. & Utomo, W. Y. Characterizing subsidence in used and restored peatland with Sentinel SAR data. *Front. Environ. Sci.* **11**, 1088923 (2023).
29. Zheng, Y., Fattahi, H., Agram, P., Simons, M. & Rosen, P. A. On Closure Phase and Systematic Bias in Multilooked SAR Interferometry. *IEEE Trans. Geosci. Remote Sens.* **60**, 1–11 (2022).
30. Liang, C. & Fielding, E. J. Interferometry With ALOS-2 Full-Aperture ScanSAR Data. *IEEE Trans. Geosci. Remote Sens.* **55**, 2739–2750 (2017).
31. Liang, C. & Fielding, E. J. Measuring azimuth deformation with L-band ALOS-2 ScanSAR interferometry. *IEEE Trans. Geosci. Remote Sens.* **55**, 2725–2738 (2017).
32. Konecny, K. et al. Variable carbon losses from recurrent fires in drained tropical peatlands. *Glob. Change Biol.* **22**, 1469–1480 (2016).

33. Putra, E. I. The effect of the precipitation pattern of the dry season on peat fire occurrence in the Mega Rice Project area, Central Kalimantan, Indonesia. *Tropics* **19**, 145–156 (2011).
34. Page, S. E. et al. The amount of carbon released from peat and forest fires in Indonesia during 1997. *Nature* **420**, 61–65 (2002).
35. Page, S. E. et al. Restoration Ecology of Lowland Tropical Peatlands in Southeast Asia: Current Knowledge and Future Research Directions. *Ecosystems* **12**, 888–905 (2009).
36. NOAA National Weather Service. Historical El Nino/La Nina episodes (-present) (1950).
37. Susilo, G. E. et al. The effect of ENSO on rainfall characteristics in the tropical peatland areas of Central Kalimantan, Indonesia. *Hydrol. Sci. J.* **58**, 539–548 (2013).
38. Khasanah, N. & van Noordwijk, M. Subsidence and carbon dioxide emissions in a smallholder peatland mosaic in Sumatra, Indonesia. *Mitig. Adapt. Strateg. Glob. Change* **24**, 147–163 (2019).
39. Evans, C. D. et al. Long-term trajectory and temporal dynamics of tropical peat subsidence in relation to plantation management and climate. *Geoderma* **428**, 116100 (2022).
40. Marshall, C. et al. Multiscale variability and the comparison of ground and satellite radar based measures of peatland surface motion for peatland monitoring. *Remote Sens* **14**, 336 (2022).
41. Rosen, P. A., Gurrola, E., Sacco, G. F. & Zebker, H. The InSAR scientific computing environment. in 730–733 (VDE, 2012).
42. Yunjun, Z., Fattahi, H. & Amelung, F. Small baseline InSAR time series analysis: Unwrapping error correction and noise reduction. *Comput. Geosci.* **133**, 104331 (2019).
43. Tough, J. A., Blacknell, D. & Quegan, S. A Statistical Description of Polarimetric and Interferometric Synthetic Aperture Radar Data. *Proc. R. Soc. Lond. Ser. Math. Phys. Sci.* **449**, 567–589 (1995).
44. Guarnieri, A. M. & Tebaldini, S. On the exploitation of target statistics for SAR interferometry applications. *IEEE Trans. Geosci. Remote Sens.* **46**, 3436–3443 (2008).
45. Milbert, D. Solid: Solid Earth Tide. (2018).
46. Yunjun, Z. et al. Range geolocation accuracy of C-/L-band SAR and its implications for operational stack coregistration. *IEEE Trans. Geosci. Remote Sens.* **60**, 1–19 (2022).
47. Liang, C., Liu, Z., Fielding, E. J. & Bürgmann, R. InSAR Time Series Analysis of L-Band Wide-Swath SAR Data Acquired by ALOS-2. *IEEE Trans. Geosci. Remote Sens.* **56**, 4492–4506 (2018).
48. Susilo, S. et al. GNSS land subsidence observations along the northern coastline of Java, Indonesia. *Sci. Data* **10**, 421 (2023).
49. NASA JPL. NASA Shuttle Radar Topography Mission Global 1 arc second. NASA Land Processes Distributed Active Archive Center https://doi.org/10.5067/MEASURES/SRTM/SRTMGL1.003 (2013).
50. Ansari, H., De Zan, F. & Parizzi, A. Study of systematic bias in measuring surface deformation with SAR interferometry. *IEEE Trans. Geosci. Remote Sens.* **59**, 1285–1301 (2020).
51. De Zan, F., Zonno, M. & Lopez-Dekker, P. Phase inconsistencies and multiple scattering in SAR interferometry. *IEEE Trans. Geosci. Remote Sens.* **53**, 6608–6616 (2015).
52. De Zan, F. & Gomba, G. Vegetation and soil moisture inversion from SAR closure phases: First experiments and results. *Remote Sens. Environ.* **217**, 562–572 (2018).
53. Bekaert, D. P. S., Walters, R. J., Wright, T. J., Hooper, A. J. & Parker, D. J. Statistical comparison of InSAR tropospheric correction techniques. *Remote Sens. Environ.* **170**, 40–47 (2015).
54. Zebker, H. A., Rosen, P. A. & Hensley, S. Atmospheric effects in interferometric synthetic aperture radar surface deformation and topographic maps. *J. Geophys. Res. Solid Earth* **102**, 7547–7563 (1997).
55. Hanssen, R. F. *Radar Interferometry: Data Interpretation and Error Analysis*. vol. **2** (Springer Science & Business Media, 2001).
56. Liu, S., Hanssen, R. & Mika, Á On the value of high-resolution weather models for atmospheric mitigation in SAR interferometry. *2009 IEEE Int. Geosci. Remote Sens. Symp.* **2**, 749 (2009).
57. Bekaert, D. P. S. et al. Development and Dissemination of Standardized Geodetic Products by the Advanced Rapid Imaging and Analysis (ARIA) Center for Natural Hazards. *Proc. Int. Union Geod. Geophys. IUGG Montr. Can.* **8**, 18 (2019).
58. Zebker, H. A. Accuracy of a model-free algorithm for temporal inSAR tropospheric correction. *Remote Sens.* **13**, 409 (2021).

Acknowledgements

The authors wish to dedicate this paper to the memory of our esteemed colleague, Dr. Susilo, who passed away during the preparation of this research. His collaboration was essential to the success of this study. We thank the Japan Aerospace Exploration Agency for the acquisition and provision of the ALOS-2 data. We also thank RISTEKDIKTI, now BRIN, for their support of the fieldwork conducted for this study, and the Head of Research and Development Centre for Environment and Forestry Banjarbaru for permission to carry out research at KHDTK Tumbang Nusa. Finally, we would like to thank the villages, farmers, and people of Kalampangan and Hampangen, Central Kalimantan, Indonesia, for the use of their sites and their support for this study. This research is supported by the National Research Foundation, Singapore, and the National Environment Agency, Singapore, under the National Sea Level Programme Funding Initiative (Award No. USS-IF-2020-5); and the Office for Space Technology and Industry (OSTIn), Singapore's national space office, through its Space Technology Development Programme (Grant No. S22-02005-STDP); and the Ministry of Education, Singapore, under its MOE AcRF Tier 3 Award MOE-MOET32022-0006 (CTP). A.J.J.-S. and C.E. acknowledge the Natural Environment Research Council for funding the NC-International programme (Grant No. NE/X006247/1) delivering National Capability. Peat cameras were initially funded by the UK Space Agency (UKSA) as part of the Peatland Assessment in SE Asia by Satellite (PASSES) project (GB-GOV-13-GCRF-UKSA_ID-MY_UKSA-08). This work comprises EOS contribution number 668.

Author contributions

Conceptualisation: S.-H.Y., C.T., C.E., A.J.J.-S. Methodology: C.T., S.-H.Y., A.J.J.-S, C.E., N.C, Y.Z. Data acquisition: C.T., A.J.J.-S, L.Y., A.J., S.S., R.S. Data processing: C.T., A.J.J.-S, L.Y., R.S., S.S. Analysis: C.T., S.-H.Y., A.J.J.-S, C.E. Original draft: C.T., C.E., S.-H.Y., A.J.J.-S. Reviewing and editing: C.T., C.E., S.-H.Y., A.J.J.-S., R.S., Y.Z., A.J., L.Y., S.D., N.C., S.S. Funding acquisition: S.H.Y., C.E., A.J.J.-S.

Competing interests

The authors declare no competing interests.

Additional information

Supplementary information The online version contains supplementary material available at https://doi.org/10.1038/s43247-025-02926-6.

Correspondence and requests for materials should be addressed to Cheryl Tay.

Peer review information *Communications Earth and Environment* thanks Rüdiger Lang, Tom Rune Lauknes, and the other, anonymous, reviewer(s) for their contribution to the peer review of this work. Primary Handling Editors: Mengze Li and Alice Drinkwater. A peer review file is available.